Raman Spectra and Strain Effects in Bismuth Oxychalcogenides

Ting Cheng,[†,‡] Congwei Tan,[†,‡] Shuqing Zhang,[∥] Teng Tu,[†] Hailin Peng,*[,†,‡,§] and Zhirong Liu*[,†,‡,§]

[†]College of Chemistry and Molecular Engineering, [‡]Center for Nanochemistry, Academy for Advanced Interdisciplinary Studies, and [§]State Key Laboratory for Structural Chemistry of Unstable and Stable Species, Beijing National Laboratory for Molecular Sciences, Peking University, Beijing 100871, China

[∥]The Low-Dimensional Materials and Devices Laboratory, Tsinghua-Berkeley Shenzhen Institute, Tsinghua University, Shenzhen 518055, Guangdong, China

Ⓢ *Supporting Information*

ABSTRACT: A new type of two-dimensional layered semiconductor with weak electrostatic but not van der Waals interlayer interactions, Bi_2O_2Se, has been recently synthesized, which shows excellent air stability and ultrahigh carrier mobility. Herein, we combined theoretical and experimental approaches to study the Raman spectra of Bi_2O_2Se and related bismuth oxychalcogenides (Bi_2O_2Te and Bi_2O_2S). The experimental peaks lie at 160 cm^{-1} in Bi_2O_2Se and at 147 and 340 cm^{-1} in Bi_2O_2Te. They were fully consistent with the calculated results (159.89, 147.48, and 340.33 cm^{-1}) and assigned to the out-of-plane A_{1g}, A_{1g}, and B_{1g} modes, respectively. Bi_2O_2S was predicted to have more Raman-active modes due to its lower symmetry. The shift in the predicted frequencies of Raman-active modes was also found to get softened as the interlayer interaction decreases from bulk to monolayer Bi_2O_2Se and Bi_2O_2Te. To reveal the strain effects on the Raman shifts, a universal theoretical equation was established based on the symmetry of Bi_2O_2Se and Bi_2O_2Te. It was predicted that the doubly degenerate modes split under in-plane uniaxial/shear strains. Under a rotated uniaxial strain, the changes in Raman shifts are anisotropic for degenerate modes, although Bi_2O_2Se and Bi_2O_2Te were usually regarded as isotropic systems similar to graphene. This implies a novel method to identify the crystallographic orientation from Raman spectra under strain. These results have important consequences for the incorporation of two-dimensional bismuth oxychalcogenides into nanoelectronic devices.
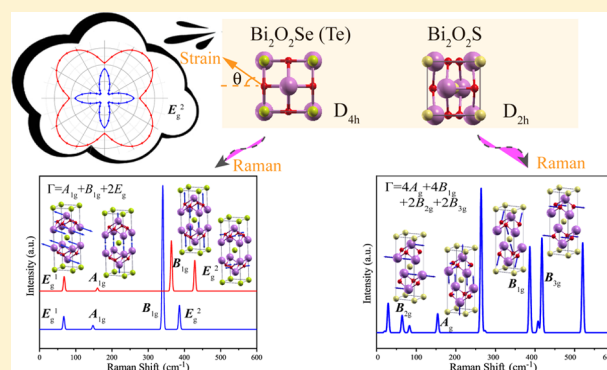
1. INTRODUCTION

With the boom in studies on two-dimensional (2D) materials, some "star materials" such as graphene,[1,2] transition-metal dichalcogenide,[3] and black phosphorene[4,5] have attracted great interest due to their fascinating properties and potential applications. They can all be categorized as van der Waals (vdW) materials considering the existence of vdW interaction between layers in their parent counterparts. Very recently, a new type of 2D material with weak interlayer electrostatic interactions instead of vdW interaction, Bi_2O_2Se, has been successfully synthesized.[6] Bi_2O_2Se was found to possess both a suitable band gap and an ultrahigh Hall mobility at low temperatures, and more importantly, to exhibit excellent environmental stability even after exposure to air for months.[6] Actually, Bi_2O_2Se was initially studied in its bulk (ceramics) form as potential n-type thermoelectric material.[7−10] After Bi_2O_2Se was synthesized into ultrathin crystal films with a thickness between tens to two layers,[6,11] it was recognized as a superior semiconductor, e.g., field-effect transistors made from it exhibit a current on/off ratio larger than 10^6 at room temperature.[6] There exists a strong spin−orbit interaction in 2D Bi_2O_2Se sheets,[12] and they were shown to have excellent optoelectronic performance as photodetectors.[13,14] The ultra-

thin thickness may also greatly enhance the thermoelectric properties.[15] Inspired by the synthesis of Bi_2O_2Se sheets, attentions were also paid to the related class of bismuth oxychalcogenides such as Bi_2O_2Te and Bi_2O_2S,[16,17] which were predicted to possess intriguing piezoelectricity and ferroelectricity.[17] They have adjustable band gaps in a range between 0.2 and 1.5 eV,[17−19] and have little mismatched lattice parameters, yielding their outstanding contributions to the 2D material family.

For the studies of 2D materials, Raman spectroscopy is a valuable tool for analyzing the structure, defect, and phase transition.[20−22] Incorporated with experimental measurements, theoretical calculations can provide additional microscopic insights that are essential for interpreting and utilizing the Raman spectroscopic information. In the previous works on the AT_2X_2 (A = K, Rb, Cs, Tl; T = Fe, Co, Ni; and X = S, Se, Te) family that adopted a tetragonal layered crystal structure (space group $I4/mmm$, No.139) similar to Bi_2O_2Se and Bi_2O_2Te, the combination of experimental and theoretical

Raman spectra shows remarkable advantages.[23−25] So far, detailed theoretical analyses of the Raman properties of the bismuth oxychalcogenides are still lacking.

This work is also motivated by the importance of strain effect. The presence of strain in low-dimensional materials modifies the crystal phonons, band structure, and carrier mobility.[26−31] The strain effects are important in understanding the performance of nanoelectronic devices, particularly in the flexible electronics. Usually, tensile strains result in mode softening, whereas compressive strains result in mode hardening. The shift in phonon frequencies with hydrostatic strain could also give the Grüneisen parameter, which is closely related to thermomechanical properties.[32] In addition, combining the applied strain and Raman shifts, one may identify the crystallographic orientation as previously shown in graphene, MoS_2, and WS_2.[27,31,33]

In this work, we studied the Raman spectra of Bi_2O_2Se, Bi_2O_2Te, and Bi_2O_2S as well as the corresponding strain effects. We first briefly discussed the geometric and electronic structures of these materials and then systematically studied the first-order Raman active modes using the group factor analysis combined with first-principle calculations and unpolarized Raman scattering experiments. To further distinguish and assign different Raman modes in the experiments, the influence of experimental geometry configuration and light polarization was also discussed here. Lastly, we explored the Raman shifts in the bulk and monolayer Bi_2O_2Se and Bi_2O_2Te with applied mechanical in-plane uniaxial/shear strains. Rotational uniaxial strain was also considered to reveal the anisotropic effect and provide a novel potential method to identify the crystallographic orientation of samples by means of the Raman shifts of split degenerate Raman modes.

2. THEORETICAL AND EXPERIMENTAL METHODS

2.1. First-Principle Calculations. The calculations of the geometric optimization and electronic structure were carried out within density functional theory, and the phonon frequencies were obtained within the density functional perturbation theory (DFPT) method implemented in Quantum Espresso package.[34] To obtain the phonon frequencies, we adopted the norm-conserving pseudopotentials with the local density approximation (LDA) exchange−correlation function, which is more suitable for phonon calculation.[35] However, the LDA usually underestimates the band gap. Therefore, to better verify the electron density used in the DFPT method, we calculated the band dispersion under LDA and compared the trend with the results using the Perdew−Burke−Ernzerhof-modified Becke−Johnson (PBE-MBJ) exchange−correlation function, which is more suitable to obtain an accurate gap.[36] For the reason of computational efficiency, we performed the MBJ calculation implemented in Vienna ab initio simulation package (VASP).[37,38] Spin−orbit coupling (SOC) effects were also considered in both LDA and PBE-MBJ calculations. In the self-consistent field calculation, the kinetic and charge density energy cutoffs were set to 80 and 320 Ry, respectively, when using the Quantum Espresso package, whereas the cutoff kinetic energy was set to 520 eV when using the VASP. The Brillouin zones were sampled with a $24 \times 24 \times 24$ and $8 \times 8 \times 1$ Monkhorst−Pack k-space mesh for the bulk primitive cell and monolayer Bi_2O_2Se and Bi_2O_2Te, respectively, and with a $27 \times 27 \times 9$ mesh for bulk Bi_2O_2S. The convergence criterion for the total energy was set

to 10^{-9} Ry and atomic forces were smaller than 10^{-5} Ry/au for the phonon calculations. For monolayer calculations, interactions between the adjacent layers were limited by setting vacuum intervals of at least 15 Å. All of the Raman spectra shown are plotted after uniform Gaussian broadening.

2.2. Material Synthesis and Spectra Measurements. The bulk Bi_2O_2Se and Bi_2O_2Te were synthesized using an oxygenation method. In this case, the O_2 was directly introduced to induce a phase transformation from Bi_2Se_3 to Bi_2O_2Se and from Bi_2Te_3 to Bi_2O_2Te (Figure S1). Herein, bulk Bi_2Se_3 and Bi_2Te_3 were employed and the trace amount of O_2 was controlled by using a gas flow meter. The pressure of the system was kept at 200 Torr and the synthesis temperature range was about 590−620 °C. Raman spectra were collected with a confocal Raman spectrometer (Jobin Yvon LabRAM HR800) using a He−Ne laser (632.8 nm).

3. RESULTS AND DISCUSSION

3.1. Geometric and Electronic Structures. We investigated three bismuth oxychalcogenide materials: Bi_2O_2Se, Bi_2O_2Te, and Bi_2O_2S. Their optimized bulk crystal structures are shown in Figure 1a−c, and all possess the inversion symmetry. The typical structures consist of stacked BiO layers sandwiched by X (X = Se, Te, and S) ions arrays with relatively weak electrostatic interactions. In each BiO layer, one O atom is bonded to four Bi atoms to form an OBi_4 tetrahedral.

Bi_2O_2Se and Bi_2O_2Te were both experimentally observed to be tetrahedral with space group $I4/mmm$,[18,39] which have ten atoms in the unit cell. Although ferroelectric phases with lower symmetry were predicted elsewhere,[17] they have not been observed in experiments yet. Here, we adopted the $I4/mmm$ symmetry as a constraint in our calculations so that the resulting Raman spectra in the figure can be used to interpret the experimental results. As seen from Figure 1a, the Se/Te atoms locate at the vertexes and the center of the cell, Bi atoms locate at the vertical edges and the vertical axis of the cell, whereas the O atoms locate at vertical middle lines of the side faces. In other words, all atoms locate at high-symmetry points or lines. However, the tetrahedral cell is not the smallest repeating unit. Actually, it is composed of two formula units. The smallest primitive unit cell is rhombohedral and contains five atoms (Figure 1b), which will be used to perform the Raman calculation. The monolayer Bi_2O_2Se and Bi_2O_2Te were also studied in our work. Following the previous experimental structure,[6] to preserve the point symmetry D_{4h} of the bulk, Se layers terminate both the top and bottom surfaces and hydrogen atoms were adopted to passivate the outermost Se layers for balancing the nonstoichiometry due to the additional Se layer (Figure 1d). The thermal stability of the monolayer Bi_2O_2Se has been verified by Yu and Sun using the ab initio molecular dynamics simulation, where it could withstand the temperature of 800 °C.[15]

Different from the highly symmetrical Bi_2O_2Se and Bi_2O_2Te, the primitive cell of bulk Bi_2O_2S is not rhombohedral but orthorhombic (with space group $Pnnm$) with anisotropic lattice parameters ($a \neq b$ in the $x−y$ plane) as revealed in the experiment.[40] S atoms still locate at the vertexes and the center of the unit cell, but Bi and O atoms all deviate from the high-symmetry lines (Figure 1c). More specifically, the upper BiO layer shifts to the left (minus x-axis) with a displacement of 0.08 Å for Bi atoms and 0.059 Å for O atoms (in our relaxed structure using LDA method), whereas the lower BiO layer shifts to the right with the same displacements. Therefore,
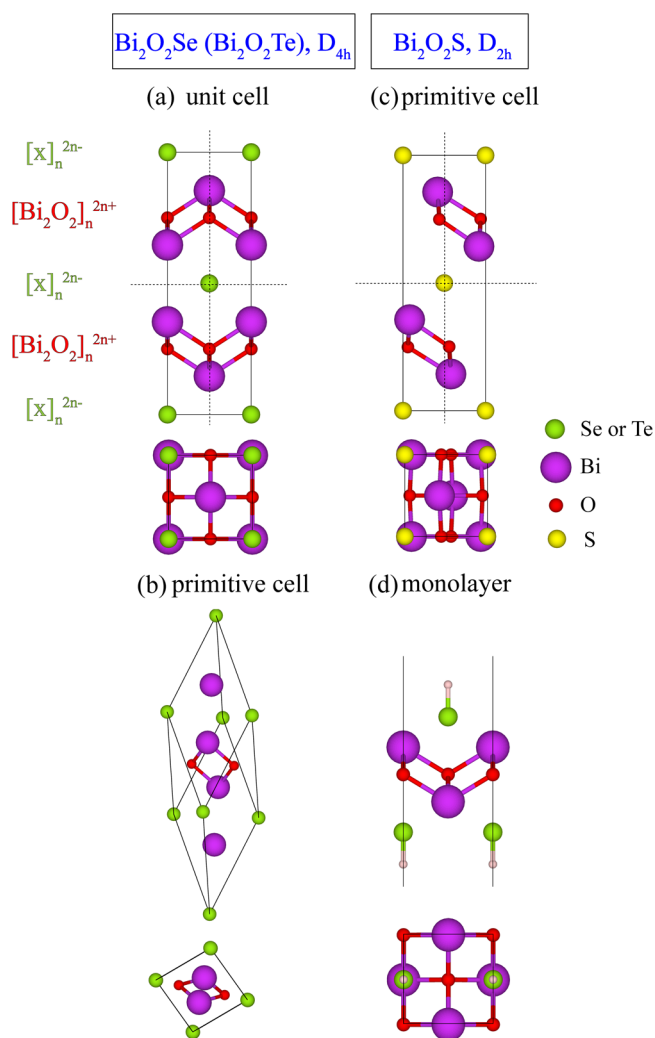
Figure 1. Geometric structures of (a) the unit cell of Bi_2O_2Se (Bi_2O_2Te), (b) the primitive cell of Bi_2O_2Se (Bi_2O_2Te) and (c) Bi_2O_2S, and (d) the monolayer of Bi_2O_2Se (Bi_2O_2Te). The dotted lines in the side view are for the convenience to mark the central axes.

Bi_2O_2S has a slightly distorted structure. The calculated lattice parameters (using both LDA and PBE method) agree to better than 2% with the experimental values,[18,39,40] which are summarized in Table 1. The lattice parameters of three systems are close, making it possible to fabricate heterostructures with little lattice mismatch.

The computed band dispersion by MBJ method is displayed in Figure 2. It indicates that three systems are all semiconductors with indirect band gaps of 0.87, 0.24, and 1.34 eV, respectively, agreeing well with the recent reported experiments on Bi_2O_2Se (0.8 eV)[6] and Bi_2O_2S (1.5 eV)[42] and previous theoretical calculations[17] (0.89, 0.16, and 1.25 eV,

respectively). Compared with the MBJ method, the LDA method gives similar band dispersion, although the gaps are obviously underestimated as usual (Figure S2).

3.2. Raman Spectra. *3.2.1. Factor Group Analysis and First-Principle Calculations.* Factor group analysis on the D_{4h} (Bi_2O_2Se, Bi_2O_2Te) and D_{2h} (Bi_2O_2S) point group yields a normal mode distribution and Raman tensors at the Brillouin zone center, which are collected in Table 2. For bulk Bi_2O_2Se and Bi_2O_2Te with D_{4h} point group symmetry, five atoms in the primitive cell result in 15 vibrational modes. Γ-point phonons could be represented by the irreducible representations of D_{4h} as: $\Gamma = A_{1g} + 3A_{2u} + B_{1g} + 2E_g + 3E_u$, where one A_{2u} and one E_u are acoustic modes, whereas A_{1g}, B_{1g}, and E_g are Raman active. The other A_{2u} and E_u are infrared active. Here, the letter "E" denotes the doubly degenerate modes in the *xy*-plane. For Bi_2O_2S crystals, due to the lower symmetry (D_{2h} point group) and more atoms (10 instead of 5) in the primitive cell, there are more vibrational modes at the Γ point: $\Gamma = 4A_g + 3A_u + 4B_{1g} + 3B_{1u} + 2B_{2g} + 6B_{2u} + 2B_{3g} + 6B_{3u}$, where one B_{1u}, one B_{2u}, and one B_{3u} are acoustic modes, whereas A_g, B_{1g}, B_{2g}, and B_{3g} are Raman modes.

The typical vibrational modes of Raman-active phonons and the predicted Raman scattering spectra of Bi_2O_2Se, Bi_2O_2Te, and Bi_2O_2S are illustrated in Figure 3. Because Bi_2O_2Se and Bi_2O_2Te share the similar structure with *I4/mmm* group symmetry, they exhibit similar vibrational modes at the Γ-point and four modes (A_{1g}, B_{1g}, E_g^1, and E_g^2) among them are Raman active. The atomic displacements associated with the Raman-active modes in the primitive and unit cells are both illustrated in Figure 3a. The A_{1g} and B_{1g} modes involve the motions of Bi and O atoms along the crystallographic *z*-axis, respectively. On the other hand, the vibrations of Bi and O atoms within the *xy*-plane give rise to two groups of degenerate E_g modes. Therefore, we may identify the A_{1g} and B_{1g} phonons as the breathing modes, whereas the two E_g modes as the interlayer shear modes. In the case of Bi_2O_2S, because of its lower symmetry, it possesses more complicated atomic motions (four A_g, four B_{1g}, two B_{2g}, and two B_{3g}) at the Γ-point. We just choose four typical modes among them, as shown in Figure 3b, which are similar to those in Bi_2O_2Se and Bi_2O_2Te. The other Raman-active modes can be found in Figure S3. The predicted Raman spectra are shown in Figure 3c. The frequencies of four Raman modes in Bi_2O_2Se are 67.99 (E_g^1), 159.89 (A_{1g}), 364.02 (B_{1g}), and 428.68 cm^{-1} (E_g^2), respectively, which are in line with the recently calculated results (72, 165.7, 369.4, and 444 cm^{-1}, using the PBE method).[43] The corresponding frequencies in Bi_2O_2Te are a litter smaller than those in Bi_2O_2Se, which are 67.01 (E_g^1), 147.48 (A_{1g}), 340.33 (B_{1g}), and 386.15 (E_g^2) cm^{-1}, respectively. For Bi_2O_2S with lower symmetry, the predicted Raman frequencies are in a sequence of 20.52 (B_{2g}), 29.23 (A_g), 64.34 (B_{2g}), 68.23 (A_g), 82.86 (A_g), 154.20 (A_g), 263.85 (B_{1g}), 273.27 (B_{3g}), 386.85 (B_{1g}), 407.76 (B_{1g}), 417.30 (B_{3g}), and 520.28 (B_{1g}) cm^{-1}. It is noted that all

Table 1. Optimized Lattice Constants for Bi_2O_2Se, Bi_2O_2Te, and Bi_2O_2S Calculated Using LDA and GGA Methods

family	atom	space group	a (Å)			b (Å)			c (Å)		
			LDA	PBE	exp[a]	LDA	PBE	exp[a]	LDA	PBE	exp[a]
Bi_2O_2S	10	*Pnnm*	3.77	3.90	3.87	3.74	3.87	3.84	11.73	12.05	11.92
Bi_2O_2Se	5	*I4/mmm*	3.83	3.92	3.88	3.83	3.92	3.88	12.02	12.38	12.16
Bi_2O_2Te	5	*I4/mmm*	3.93	4.01	3.98	3.93	4.01	3.98	12.54	12.88	12.70

[a]The experimental values of Bi_2O_2S, Bi_2O_2Se, and Bi_2O_2Te were adopted from refs 40, 39, and 18, respectively, to provide a comparision.
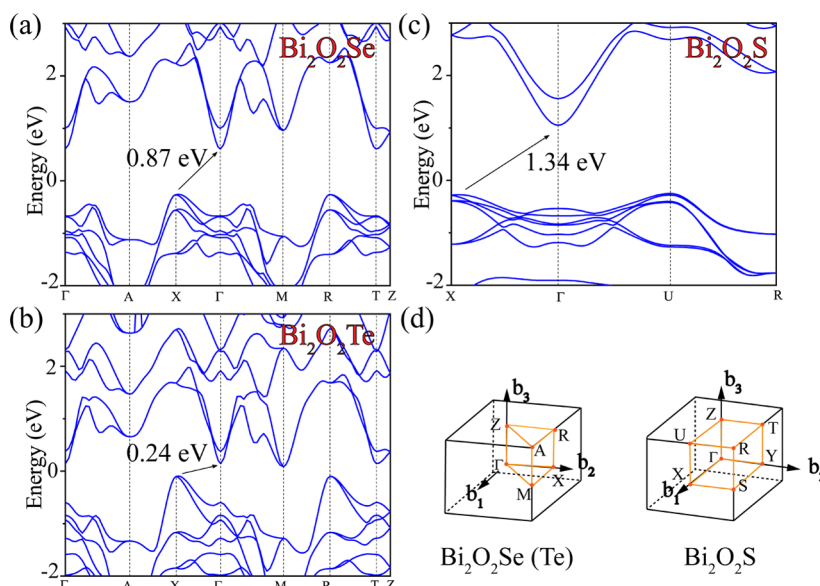
Figure 2. Electronic band structures of (a) Bi_2O_2Se, (b) Bi_2O_2Te, (c) Bi_2O_2S and (d) their corresponding first Brillouin zone (following the notation rules in ref 41) calculated by the MBJ method. The SOC effect was considered here.

Table 2. Types of Atoms Together with Their Wyckoff Positions and Each Site's Irreducible Representations in the Γ-Point Phonons, as Well as Raman Tensors, Phonon Activites, and Selection Rules for Bi_2O_2Se (Bi_2O_2Te) and Bi_2O_2S

Bi_2O_2Se (Te)

Atoms	Wyckoff position	Irreducible representations
Bi	$4e$ $(0, 0, z)$	$A_{1g} + A_{2u} + E_g + E_u$
O	$4d$ $(0, 1/2, 1/4)$	$B_{1g} + A_{2u} + E_g + E_u$
Se/ Te	$2a$ $(0, 0, 0)$	$A_{2u} + E_u$

Raman Tensors

$$\hat{R}_{A_{1g}} = \begin{pmatrix} a & 0 & 0 \\ 0 & a & 0 \\ 0 & 0 & b \end{pmatrix} \quad \hat{R}_{B_{1g}} = \begin{pmatrix} c & 0 & 0 \\ 0 & -c & 0 \\ 0 & 0 & 0 \end{pmatrix} \quad \hat{R}_{E_g^1} = \begin{pmatrix} 0 & 0 & e \\ 0 & 0 & 0 \\ e & 0 & 0 \end{pmatrix} \quad \hat{R}_{E_g^2} = \begin{pmatrix} 0 & 0 & 0 \\ 0 & 0 & f \\ 0 & f & 0 \end{pmatrix}$$

Activity and selection rules

$$\Gamma_{\text{Raman-active}} = A_{1g}(\alpha_{xx+yy}, \alpha_{zz}) + 2E_g(\alpha_{xz}, \alpha_{yz}) + B_{1g}(\alpha_{xx} - \alpha_{yy})$$

$$\Gamma_{\text{acoustic}} = A_{2u} + E_u$$

Bi_2O_2S

Atoms	Wyckoff position	Irreducible representations
Bi, O	$4g$ $(x, y, 0)$	$2A_g + A_{2u} + 2B_{1g} + B_{2g} + B_{1u} + 2B_{2u} + B_{3g}$
S	$2a$ $(0, 0, 0)$	$B_{1u} + A_u + 2B_{2u} + 2B_{3u}$

Raman Tensors

$$\hat{R}_{A_g} = \begin{pmatrix} a & 0 & 0 \\ 0 & b & 0 \\ 0 & 0 & c \end{pmatrix} \quad \hat{R}_{B_{1g}} = \begin{pmatrix} 0 & d & 0 \\ d & 0 & 0 \\ 0 & 0 & 0 \end{pmatrix} \quad \hat{R}_{B_{2g}} = \begin{pmatrix} 0 & 0 & e \\ 0 & 0 & 0 \\ e & 0 & 0 \end{pmatrix} \quad \hat{R}_{B_{3g}} = \begin{pmatrix} 0 & 0 & 0 \\ 0 & 0 & f \\ 0 & f & 0 \end{pmatrix}$$

Activity and selection rules

$$\Gamma_{\text{Raman-active}} = 4A_g(\alpha_{xx}, \alpha_{yy}, \alpha_{zz}) + 4B_{1g}(\alpha_{xy}) + 2B_{2g}(\alpha_{xz}) + 2B_{3g}(\alpha_{yz})$$

$$\Gamma_{\text{acoustic}} = B_{1u} + B_{2u} + B_{3u}$$

Raman-active vibrations come from the BiO layer, whereas there is no contribution from Se, Te, or S atoms. Therefore, the Raman frequencies of three systems nearly appear in the same range (<600 cm^{-1}). Besides, the predicted peak intensity is expected to be less accurate than the frequency because the experimental peak intensity is usually affected by many factors,

such as the substrate, the energy of the incident light, and so on.

3.2.2. Experimental Confirmations. In general, whether a Raman mode in crystals could be observed in experiments is determined by its Raman tensor and the experimental configuration. In the usual backscattering configuration, one can only observe two intrinsic Raman peaks (A_{1g} and B_{1g}) for
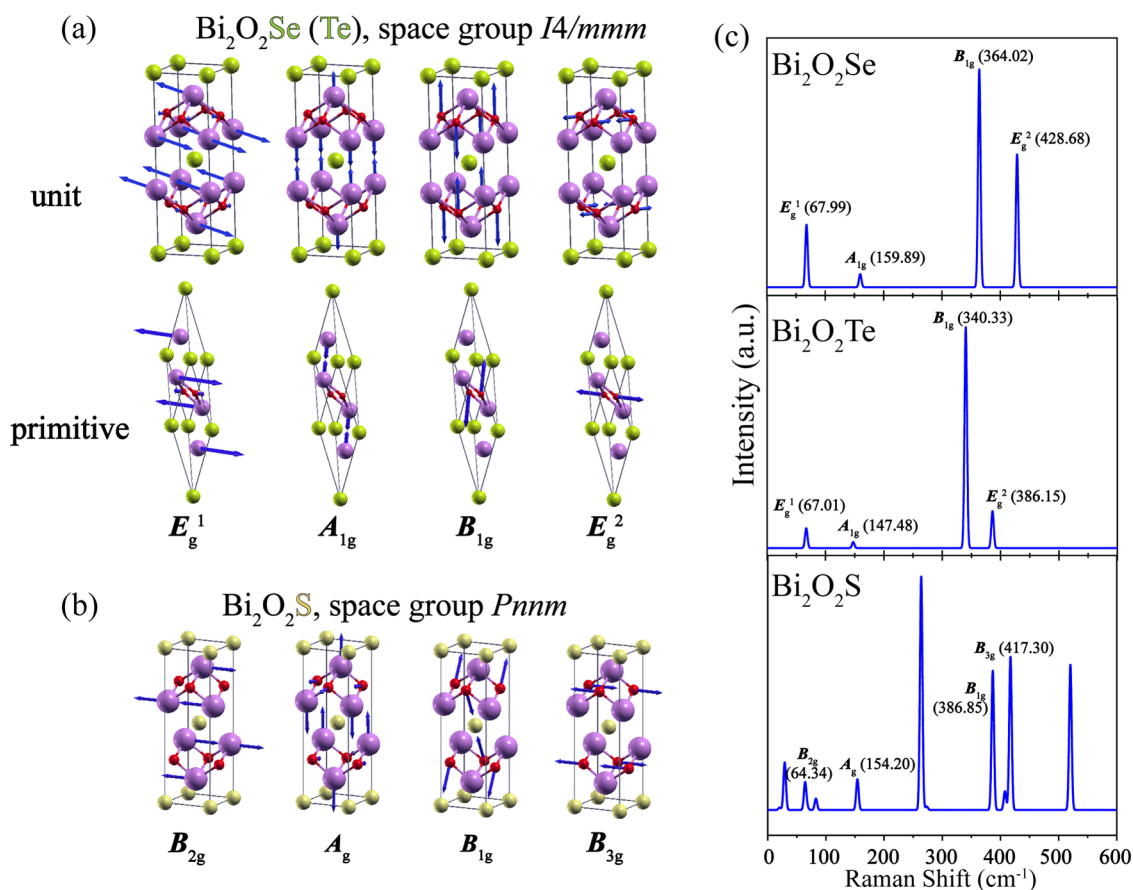
Figure 3. Raman spectra of bismuth oxychalcogenides. (a) The atomic displacements of all Raman-active vibrational modes in Bi_2O_2Se (Bi_2O_2Te) with a unit cell (top) or a primitive cell (bottom). (b) Four typical Raman-active modes in Bi_2O_2S, which are similar to those in Bi_2O_2Se (Bi_2O_2Te), whereas the other Raman-active modes can be found in Figure S3. (c) The predicted Raman spectra of Bi_2O_2Se, Bi_2O_2Te, and Bi_2O_2S. The frequencies of presented Raman modes in (a, b) are labeled in (c).
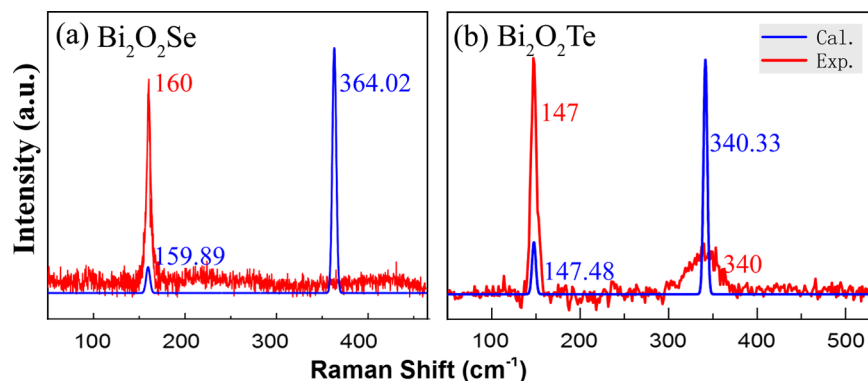
Figure 4. Unpolarized Raman scattering spectra of (a) Bi_2O_2Se and (b) Bi_2O_2Te sheet samples (red) measured at room temperature in a backscattering configuration compared with the theoretical results (blue). The frequencies of peaks are labeled.

Bi_2O_2Se and Bi_2O_2Te according to the Raman tensors shown in Table 2, whereas only the A_g and B_{1g} modes (eight peaks) are expected to be observed for Bi_2O_2S. The observation of the E_g modes for Bi_2O_2Se (Bi_2O_2Te) or the B_{2g} and B_{3g} modes for Bi_2O_2S requires measurement in the xz- or yz-planes of the sample, which would be hard for thin 2D sheets but easy for bulk samples.

A comparison between the experimental results and the predictions is provided in Figure 4 for the unpolarized Raman spectra of Bi_2O_2Se and Bi_2O_2Te in a backscattering configuration. The experimental peaks located at about 160

cm^{-1} in Bi_2O_2Se and 147 cm^{-1} in Bi_2O_2Te could be assigned as the A_{1g} mode, which are in good agreement with our predictions (159.89 and 147.48 cm^{-1}, respectively). The experimental peak at the 340 cm^{-1} in Bi_2O_2Te (which is much less sharp) could be assigned as the B_{1g} mode, also being consistent with the prediction (340.83 cm^{-1}). In the experiment, we did not observe a peak near 364 cm^{-1} (the predicted B_{1g} mode) in Bi_2O_2Se. It is unclear whether the B_{1g} peak is absent because the intensity is too weak (noting that the detected intensity of the B_{1g} mode is much lower than that of the A_{1g} mode in Bi_2O_2Te) or for other unknown reasons. In

Table 3. Calculated and Experimental Raman Frequencies for Bi_2O_2Se, Bi_2O_2Te, Bi_2Se_3, and Bi_2Te_3[a]

| | Bi_2O_2Se (Bi_2O_2Te) space group $I4/mmm$ | | | | Bi_2Se_3 (Bi_2Te_3) space group $R\bar{3}m$ | | | |
	E_g^1	A_{1g}	B_{1g}	E_g^2	E_g	A_{1g}	E_g	A_{1g}
fully relaxed	72.21 (72.84)	166.83 (154.25)	376.20 (352)	449.60 (408.03)	44.4 (43.2)	75 (64.4)	142.7 (112.8)	180.6 (140.8)
partially relaxed	67.99 (67.01)	159.89 (147.48)	364.02 (340.33)	428.68 (386.15)	40.4 (40)	68 (58.8)	135 (108.9)	174.2 (138.5)
exp[b]		160 (147)	(340)		37 (36)	69 (62)	131 (102)	174 (133)

[a]The frequencies for Bi_2O_2Te and Bi_2Te_3 are listed in brackets. The structures were fully or partially relaxed depending on whether the lattice parameters were fixed to the experimental values in calculations or not, resulting in different frequency values as listed. [b]The frequency values of Bi_2O_2Se and Bi_2O_2Te are chosen from our experiments. And, the experimental values of Bi_2Se_3 and Bi_2Te_3 are chosen from refs 47 and 48, respectively.

a recent study of Bi_2O_2Se under high pressure by Pereira et al., the B_{1g} mode was also not observed in the Raman spectrum measurement and only A_{1g} mode (at about 159.2 cm^{-1}) existed.[43] They explained the absence of the B_{1g} mode in terms of the plasmon−phonon coupling L$^+$ or L$^-$ band of the B_{1g} mode caused by the large carrier concentration in n-type semiconductor.[43] According to previous Raman experiments and calculations on AT_2X_2 structures with $I4/mmm$ symmetry (such as iron-chalcogenide compounds), defects such as vacancy ordering, consequently, symmetry lowering may lead to the appearance of additional Raman peaks.[24,44,45] As an evidence, in a previous high-quality Bi_2O_2Se sample, only one Raman peak located at about 160 cm^{-1} was reported,[11] which can be assigned to the A_{1g} mode. In the current case, no additional peaks other than the intrinsic Raman peaks were observed, indicating the high quality of our synthesized sample. On this occasion, the reason for the disappearance of B_{1g} in Bi_2O_2Se requires further verification of experimental and theoretical studies.

A better way to distinguish and assign different Raman modes in the experiments is to adopt polarized configurations. According to the selection rules, the A_g and B_{1g} modes of Bi_2O_2S could be easily distinguished in parallel and crossed polarization configurations, whereas more complicated configurations are required to distinguish the A_{1g} and B_{1g} modes in Bi_2O_2Se and Bi_2O_2Te (see the Supporting Information Figure S4 for more details). Raman modes in similar systems AT_2X_2 (with $I4/mmm$ group symmetry) have been successfully distinguished with such an approach.[24,46] Limited by the current sample condition, we did not pursue polarized Raman experiments here.

To further verify the reliability of the calculation methods, we performed extra calculations on Bi_2Se_3 and Bi_2Te_3 to compare with the reported experimental results.[47,48] The Raman frequencies are usually sensitive to the values of lattice constants. Therefore, two schemes of structural optimization were adopted in our calculations. In the first scheme, the structure was fully relaxed, where both the lattice constants and the atomic coordinates were optimized. In the second scheme, the structure was partially relaxed, where only the atomic positions were optimized, whereas the lattice parameters were kept at their experimental values. Similar schemes were also applied for Bi_2O_2Se and Bi_2O_2Te. The obtained results are summarized in Table 3. It can be seen that the values obtained with fully relaxed structures are obviously larger than the experimental values, owing to the fact that LDA usually underestimates the lattice parameters. In comparison, the results obtained under the partially relaxed structure (with experimental lattice constants) are more consistent with the observed values, with an average deviation as small as 3.5 cm^{-1}. Similar trend was also found in other systems such as MoS_2.[49]

Therefore, to compare with the Raman experiments, it is better to adopt the experimental lattice parameters in calculations. The calculated Raman spectra in Figures 3 and 4 for Bi_2O_2Se and Bi_2O_2Te also adopted such a scheme.

Apart from the bulk materials, we calculated the Raman frequencies in fully relaxed monolayer Bi_2O_2Se and Bi_2O_2Te. The resulting frequencies are 80.44, 153.59, 366.10, and 409.95 cm^{-1} for Bi_2O_2Se and 59.20, 141.10, 340, and 364.35 cm^{-1} for Bi_2O_2Te, all exhibiting redshifts from the bulk except the ^1E_g mode (80.44 vs 72.21 cm^{-1}) in Bi_2O_2Se. Similar mode softening has also been found in many vdW layer materials such as Bi_2Se_3 and Bi_2Te_3, which may be explained by the weaker interlayer restoring forces in the vibrations when the number of layer decreases.[47,48]

3.3. Strain Dependence of Raman Spectra. In this section, we theoretically investigated the Raman shift of monolayer and bulk Bi_2O_2Se and Bi_2O_2Te (all with D_{4h} symmetry) under the mechanical in-plane strain. The applied strain tensor is written as

$$\boldsymbol{\varepsilon} = \begin{bmatrix} \varepsilon_{xx} & \gamma \\ 0 & \varepsilon_{yy} \end{bmatrix} \tag{1}$$

where ε_{xx} and ε_{yy} represent the uniaxial strain along the x- and y-directions, respectively, and γ is the engineering shear strain related to the usual (symmetric) shear strain ε_{xy} as $\gamma = 2\varepsilon_{xy}$.[30] Here, we focus on the linear effect of strain on vibration frequencies.

3.3.1. In-Plane Uniaxial and Shear Strain. The Raman frequency ω is a function of applied strain ε. For a nondegenerate vibrational mode such as A_{1g} and B_{1g}, the frequency ω could be generally expanded as a Taylor series of ε components

$$\omega(\varepsilon_{xx}, \varepsilon_{yy}, \gamma) = \omega_0 + k_x\varepsilon_{xx} + k_y\varepsilon_{yy} + k_\gamma\gamma$$
$$+ \text{(high-order terms)} \tag{2}$$

where k_x, k_y, and k_γ are the linear coefficients, which could be determined by separately applying the strain ε_{xx}, ε_{yy}, and γ. Under the D_{4h} symmetry of Bi_2O_2Se and Bi_2O_2Te, the x-axis and y-axis are equivalent, which requires that $k_x = k_y \equiv \bar{k}$. Moreover, under a mirror reflection with a normal direction along the x- or y-axis, γ changes into $-\gamma$, and the symmetry requires that $k_\gamma = 0$. Therefore, with the D_{4h} symmetry, eq 2 is simplified into

$$\omega(\varepsilon_{xx}, \varepsilon_{yy}, \gamma) = \omega_0 + \bar{k}(\varepsilon_{xx} + \varepsilon_{yy}) + \text{(high-order terms)} \tag{3}$$

with only one independent parameter $\bar{k}$ under the linear expansion. When the mode is degenerate, it will split into two bands under strains and the relationship between ω and ε
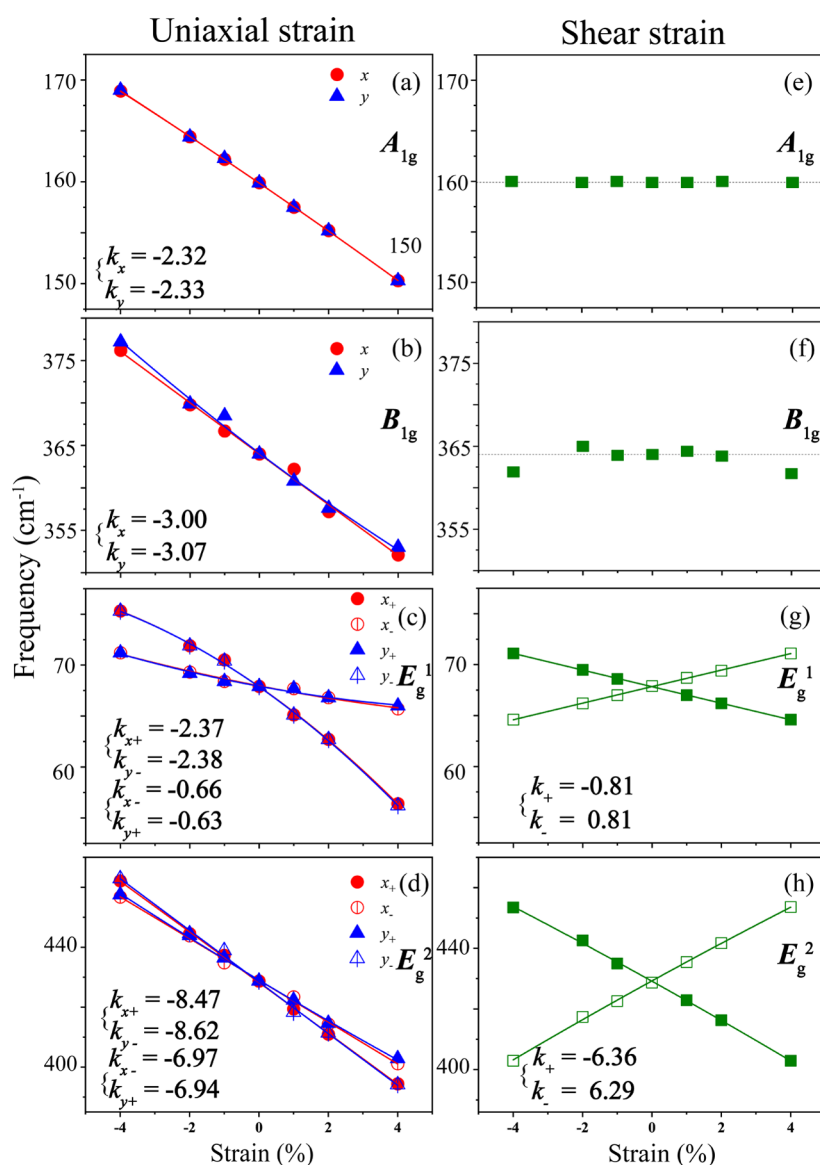
Figure 5. Evolutions of Raman shift with (a−d) uniaxial strain and (e−h) shear strain for bulk Bi_2O_2Se. The calculated data points (squares and triangles) are fitted with a parabolic equation (solid lines) and the fitted linear coefficients (unit: $cm^{-1}/\%$) are also shown in the panels. Red and blue are used to denote the results under ε_{xx} and ε_{yy}, respectively. For the degenerate modes, the open and filled symbols are used to distinguish the two splitting frequencies under the uniaxial strain.

should be analyzed by examining the strain response of the corresponding Hamiltonian.[50] Under the D_{4h} symmetry, the splitting of degenerate modes such as E_g is given as (the detailed deduction is given in the Supporting Information)

$$\omega_{1,2}(\varepsilon_{xx}, \varepsilon_{yy}, \gamma) = \omega_0 + \bar{k}(\varepsilon_{xx} + \varepsilon_{yy})$$
$$\pm \sqrt{[\Delta k(\varepsilon_{xx} - \varepsilon_{yy})]^2 + (k_\gamma \gamma)^2}$$
$$+ \text{(high-order terms)} \qquad (4)$$

where $\bar{k}$, Δk, and k_γ are three independent parameters under the D_{4h} symmetry. It is noted that the number of independent parameters is determined by the symmetry. For example, graphene, graphyne, and graphdiyne have a higher symmetry (D_{6h}), so $\Delta k = k_\gamma$ and there are only two independent parameters for strain effect of E_g mode.[50]

We conducted first-principle calculations on monolayer and bulk Bi_2O_2Se and Bi_2O_2Te with various ε_{xx}, ε_{yy}, and γ strains

up to ±4%. Before discussing the behaviors of the Raman spectrum, we first briefly survey the mechanical properties of the studied systems. The elastic constant C_{11} is critical in determining the mobility.[51,52] The calculated C_{11} of the monolayer Bi_2O_2Se was 100 J m^{-2} (see Figure S5 for the fitted curve), which compares well to the previous calculation with the PBE method (92 J m^{-2}).[15] For the monolayer Bi_2O_2Te, it was a little smaller, 95 J m^{-2}. The shear modulus C_{66} of these two materials is 54 and 50 J m^{-2}, respectively. The obtained C_{11} of the monolayers Bi_2O_2Se and Bi_2O_2Te is only about one-third that of graphene (358 J m^{-2})[53] and smaller than that of graphyne (207 J m^{-2}), graphdiyne (159 J m^{-2}), or 8B-*Pmmn* borophene (253 J m^{-2}).[50,54] But, it is comparable or even higher than that of monolayer black phosphorous (29 and 102 J m^{-2} along the *x*- and *y*-direction, respectively).[55]

The calculated shift and splitting of Raman frequencies under various strains are displayed in Figure 5 for bulk Bi_2O_2Se. The data points were fitted with parabolic curves, and

Table 4. Determined Coefficient $\bar{k}$, Δk, and k_γ (in Units of cm^{-1}/%) for Four Raman-Active Modes in Bulk and Monolayer Bi$_2$O$_2$Se and Bi$_2$O$_2$Te under Applied Strains

		E_g^1			A_{1g}	B_{1g}	E_g^2		
		$\bar{k}$	Δk	k_γ	$\bar{k}$	$\bar{k}$	$\bar{k}$	Δk	k_γ
Bi$_2$O$_2$Se	bulk	−1.51	0.85	0.81	−2.33	−3.04	−7.72	0.75	6.33
	mono	−2.15	0.43	1.86	−2.31	−1.65	−5.97	0.56	6.59
Bi$_2$O$_2$Te	bulk	−1.88	0.95	1.05	−2.32	−3.53	−7.68	0.93	5.78
	mono	−1.61	0.41	1.56	−2.32	−1.67	−6.07	0.31	6.38
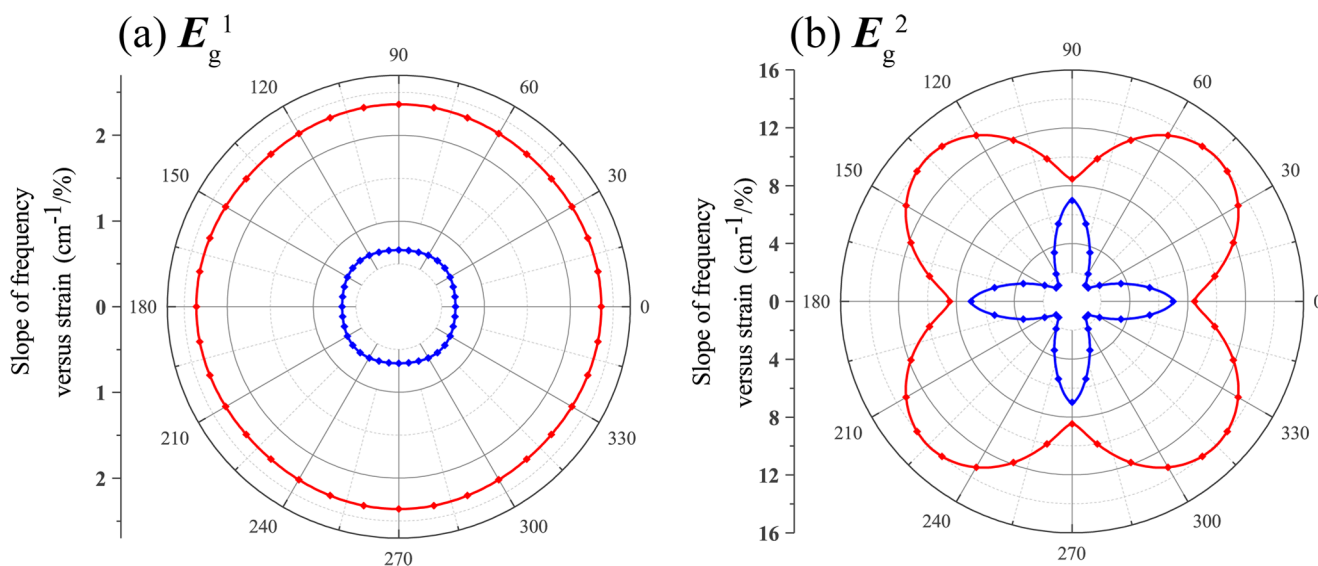
Figure 6. Changes in Raman frequencies under a rotated uniaxial strain for degenerate (a) E_g^1 and (b) E_g^2 modes in bulk Bi$_2$O$_2$Se. The data were calculated from eq 9, with the values of $\bar{k}$, Δk, and k_γ listed in Table 4. Red and blue lines represent k_1 and k_2 for two splitting bands, respectively.

the resulting linear coefficients (slopes) are listed in the figure. The fitting works well. Under the D_{4h} symmetry, the x- and y-directions are equivalent. For nondegenerate modes, the slopes with respect to ε_{xx} and ε_{yy} were practically identical (−2.32 ≈ −2.33 for A_{1g} mode and −3.00 ≈ −3.07 for B_{1g} mode), consistent with the analysis in eq 3. For each doubly degenerate E_g mode, it splits into two branches and gives four linear coefficients under ε_{xx} and ε_{yy} in a direct fitting. They are well grouped into two values (e.g., −2.37 ≈ −2.38 and −0.66 ≈ −0.63 for E_g^1 mode), which agrees well with our eq 4 and can be combined to give $\bar{k}$ and Δk. Overall, all Raman modes show redshifts under tensile strains and blueshifts under compressive strains. The E_g^2 mode shows the largest slope, indicating that it is the most affected under uniaxial strain. Different from the effect of uniaxial strain in which two splitting branches of doubly degenerate E_g modes always shift along the same direction, a shear strain would soften one branch but harden another with opposite slopes (Figure 5g,h), as predicted by eq 4. The nondegenerate nodes A_{1g} and B_{1g} are unaffected by shear strain.

We have systematically investigated the strain effects in Bi$_2$O$_2$Se and Bi$_2$O$_2$Te in both bulk and monolayer forms. Detailed calculated results are shown in Figures S6−S8, and the extracted coefficients $\bar{k}$, Δk, and k_γ are summarized in Table 4. The coefficients of Bi$_2$O$_2$Se are close to those of Bi$_2$O$_2$Te both in the bulk form and the monolayer form owing to their similar structures and vibration modes. For differences between the bulk and the monolayer, the coefficients for the B_{1g} mode in monolayer are obviously smaller than those in the

bulk form, whereas the coefficients for the A_{1g} mode remain nearly unchanged.

The above extracted coefficients of phonon shift under strains could give the Grüneisen parameter γ_m, which is related to thermodynamic properties and has been discussed in isotropic 2D materials such as graphene and 2H-MoS$_2$.[27,28] The Grüneisen parameter for a mode m, γ_m, is defined as[32]

$$\gamma_m = -\frac{1}{\omega_m}\frac{\partial \omega_m}{\partial \varepsilon}$$

where the strain $\varepsilon = \varepsilon_{xx} + \varepsilon_{yy}$ is the hydrostatic component of the applied uniaxial strain. Therefore, based on eqs 3 and 4, we have $\gamma_m = -\bar{k}/\omega_m$ for both degenerate and nondegenerate modes. Then, γ_m that we found for each mode were 2.67, 1.50, 0.45, and 1.46 for ^1E_g, A_{1g}, B_{1g}, and ^2E_g modes in monolayer Bi$_2$O$_2$Se, respectively, and 2.72, 1.64, 0.49, and 1.67 for monolayer Bi$_2$O$_2$Te. These values are comparable to those for the G ($\gamma_m = 1.72$) and 2D ($\gamma_m = 2.0$) peaks of graphene[27,56] and larger than those in the monolayer 2H-MoS$_2$ (0.54, 0.65, and 0.21 for E″, E′, and A$_1'$ modes, respectively).[28]

3.3.2. In-Plane Rotated Uniaxial Strain. When a uniaxial strain with a magnitude ε is applied along a direction with angle θ to the x-axis, the stain tensor can be expressed by a rotation transformation as

$$\boldsymbol{\varepsilon}(\varepsilon, \theta) = \begin{bmatrix} \varepsilon_{xx} & \varepsilon_{xy} \\ \varepsilon_{xy} & \varepsilon_{yy} \end{bmatrix} = \mathbf{R}^{\mathrm{T}} \begin{bmatrix} \varepsilon & 0 \\ 0 & 0 \end{bmatrix} \mathbf{R}$$

$$= \begin{bmatrix} \varepsilon \cos^2 \theta & -\varepsilon \sin \theta \cos \theta \\ -\varepsilon \sin \theta \cos \theta & \varepsilon \sin^2 \theta \end{bmatrix} \quad (5)$$

where $\mathbf{R}$ is the 2D rotation matrix

$$\mathbf{R} = \begin{bmatrix} \cos \theta & -\sin \theta \\ \sin \theta & \cos \theta \end{bmatrix} \quad (6)$$

We could then obtain the variation in Raman frequencies under a rotated uniaxial strain by substituting eq 5 into eqs 3 and 4. Considering the linear effects, for a nondegenerate vibrational mode, eq 3 evolves into

$$\omega(\varepsilon, \theta) = \omega_0 + \bar{k}\varepsilon \quad (7)$$

Therefore, the strain effect on nondegenerate modes such as A_{1g} and B_{1g} is isotropic, i.e., the Raman frequencies do not depend on the direction of strain, which is different from anisotropic systems such as black phosphorus.[29] For degenerate modes such as ^1E_g and ^2E_g, eq 4 evolves into

$$\omega_{1,2}(\varepsilon, \theta) = \omega_0 + \{k \pm \sqrt{[\Delta k \cos(2\theta)]^2 + [k_\gamma \sin(2\theta)]^2}\}\varepsilon \quad (8)$$

taking into account $\gamma = 2\varepsilon_{xy}$. Hence, the change rate of the frequency versus strain is angle-dependent

$$k_{1,2} = \frac{\partial \omega_{1,2}}{\partial \varepsilon} = \bar{k} \pm \sqrt{[\Delta k \cos(2\theta)]^2 + [k_\gamma \sin(2\theta)]^2} \quad (9)$$

The change rates of Raman frequencies under a rotating strain for Bi_2O_2Se are demonstrated in Figure 6. It was recognized from eq 4 that the anisotropy depends on the relative values between Δk and k_γ. For the E_g^1 mode, the anisotropy is weak (Figure 6a) because its Δk and k_γ are close (0.85 vs 0.81). In contrast, Δk and k_γ are markedly different (0.75 vs 6.33) for the E_g^1 mode, so the resulting anisotropic effect is strong (Figure 6b). Such a difference may originate from the fact that the E_g^2 mode is an in-plane vibration and more sensitive to the applied strain, whereas the E_g^1 mode involves the motion of interlayer Bi atoms. The anisotropic effects under a rotated strain were also found in the monolayer Bi_2O_2Se and Bi_2O_2Te as shown in the Supporting Information (Figure S9). It is worth noting that the degenerate E_g modes in graphene or graphynes also split under a uniaxial strain, but the frequencies therein are isotropic because they have $\Delta k = k_\gamma$ due to the symmetry.

The anisotropic strain effect can be utilized to determine the crystallographic orientation of Bi_2O_2Se and Bi_2O_2Te in the experiments. When an experimental sample is stretched along a fixed direction, $k_{1,2}$ can be readily measured as the ratio between the change in frequency and the magnitude of strain, and then the orientation angle θ can be solved from eq 9 with the known parameters $\bar{k}$, Δk, and k_γ listed in Table 4. A practical scheme is provided here. Denote

$$\begin{cases} a = \cos^2(2\theta) \\ b = \sin^2(2\theta) \end{cases} \quad (10)$$

then, a recombination of eq 9 gives

$$\begin{bmatrix} (k_1 - k_2)^2 \\ (k_1 + k_2)^2 \end{bmatrix} = \begin{bmatrix} (\Delta k)^2 & (k_\gamma)^2 \\ \bar{k}^2 & \bar{k}^2 \end{bmatrix} \begin{bmatrix} a \\ b \end{bmatrix} \quad (11)$$

After a and b are solved from eq 11, θ is determined to be

$$\theta = \begin{cases} 0° & (\text{if } b < 0) \\ 45° & (\text{if } a < 0) \\ \dfrac{1}{2}\arccos\sqrt{\dfrac{a}{a + b}} & (\text{otherwise}) \end{cases} \quad (12)$$

The strain efficiency, i.e., the efficiency of a strain to transfer from the substrate to the sample, does not affect the accuracy of θ determined as in the previous study on black phosphorus.[29]

4. CONCLUSIONS

In summary, based on the group-theory analysis and first-principles calculations, we predicted the Raman spectra of Bi_2O_2Se, Bi_2O_2S, and Bi_2O_2Te and determined their response to mechanical strain. Bi_2O_2Se and Bi_2O_2Te share the similar structure with D_{4h} point symmetry and four Raman-active modes (A_{1g}, B_{1g}, and E_g^2). The experimental work was carried out to give the Raman spectra of Bi_2O_2Se and Bi_2O_2Te. The observed peaks (160 cm^{-1} in Bi_2O_2Se and 147 and 340 cm^{-1} in Bi_2O_2Te) were fully consistent with the calculated results (159.89, 147.48, and 340.33 cm^{-1}) and assigned to the out-of-plane A_{1g}, A_{1g}, and B_{1g} modes, respectively. Bi_2O_2S, on the other hand, possesses a lower symmetry (D_{2h}) and more atoms in its unit cell, so it has more Raman-active modes ($4A_g$, $4B_{1g}$, $2B_{2g}$, and $2B_{3g}$). From bulk to the monolayer Bi_2O_2Se and Bi_2O_2Te, most Raman frequencies show redshift, which may result from the decrease in the interlayer interactions as that in other 2D materials. To reveal the strain effects on the Raman shifts, a universal theoretical equation was established based on the D_{4h} symmetry. All Raman modes show redshifts under tensile strain. The doubly degenerate modes split under uniaxial and shear strains. Under a rotated uniaxial strain, the frequency variation in degenerate modes is anisotropic, although the x- and y-axes are equivalent under the D_{4h} symmetry, in contrast to the isotropic case of graphene with the D_{6h} symmetry. This provides a novel method to identify the crystallographic orientation of the D_{4h} system by measuring the changes in degenerate Raman modes under applied uniaxial strains. Overall, the changes in Raman shift under strain and the good match in the lattice constants are beneficial for bismuth oxychalcogenides-based nanoelectronics and mechanical systems.

■ ASSOCIATED CONTENT

ⓢ Supporting Information

The Supporting Information is available free of charge on the ACS Publications website at DOI: 10.1021/acs.jpcc.8b05475.

SEM imagining, calculated band structure using the LDA method, remaining Raman-active modes in Bi_2O_2S, polarization configuration in theory, detailed deducing process of equations, calculated 2D elastic constant, and remaining evolutions of Raman shifts with strain (PDF)

■ AUTHOR INFORMATION

Corresponding Authors
*E-mail: hlpeng@pku.edu.cn (H.P.).
*E-mail: LiuZhiRong@pku.edu.cn (Z.L.).

ORCID ⊙

Ting Cheng: 0000-0002-6204-2201
Hailin Peng: 0000-0003-1569-0238

Author Contributions

The manuscript was written through contributions of all the authors. All the authors have given approval to the final version of the manuscript.

Notes

The authors declare no competing financial interest.

■ REFERENCES

(1) Geim, A. K.; Novoselov, K. S. The rise of graphene. *Nat. Mater.* **2007**, *6*, 183.

(2) Novoselov, K. S.; Geim, A. K.; Morozov, S. V.; Jiang, D.; Katsnelson, M. I.; Grigorieva, I. V.; Dubonos, S. V.; Firsov, A. A. Two-dimensional gas of massless Dirac fermions in graphene. *Nature* **2005**, *438*, 197.

(3) Chhowalla, M.; Shin, H. S.; Eda, G.; Li, L. J.; Loh, K. P.; Zhang, H. The chemistry of two-dimensional layered transition metal dichalcogenide nanosheets. *Nat. Chem.* **2013**, *5*, 263.

(4) Kaur, S.; Kumar, A.; Srivastava, S.; Pandey, R.; Tankeshwar, K. Stability and carrier transport properties of phosphorene-based polymorphic nanoribbons. *Nanotechnology* **2018**, *29*, No. 155701.

(5) Li, X. J.; Yu, J. H.; Luo, K.; Wu, Z. H.; Yang, W. Tuning the electrical and optical anisotropy of a monolayer black phosphorus magnetic superlattice. *Nanotechnology* **2018**, *29*, No. 174001.

(6) Wu, J.; Yuan, H. T.; Meng, M. M.; Chen, C.; Sun, Y.; Chen, Z. Y.; Dang, W. H.; Tan, C. W.; Liu, Y. J.; Yin, J. B.; et al. High electron mobility and quantum oscillations in non-encapsulated ultrathin semiconducting Bi$_2$O$_2$Se. *Nat. Nanotechnol.* **2017**, *12*, 530.

(7) Ruleova, P.; Drasar, C.; Lostak, P.; Li, C. P.; Ballikaya, S.; Uher, C. Thermoelectric properties of Bi$_2$O$_2$Se. *Mater. Chem. Phys.* **2010**, *119*, 299.

(8) Tan, X.; Lan, J. L.; Ren, G. K.; Liu, Y. C.; Lin, Y. H.; Nan, C. W. Enhanced thermoelectric performance of n-type Bi$_2$O$_2$Se by Cl-doping at Se site. *J. Am. Ceram. Soc.* **2017**, *100*, 1494.

(9) Tan, X.; Liu, Y. C.; Hu, K. R.; Ren, G. K.; Li, Y. M.; Liu, R.; Lin, Y. H.; Lan, J. L.; Nan, C. W. Synergistically optimizing electrical and thermal transport properties of Bi$_2$O$_2$Se ceramics by Te-substitution. *J. Am. Ceram. Soc.* **2018**, *101*, 326.

(10) Zhan, B.; Liu, Y. C.; Tan, X.; Lan, J. L.; Lin, Y. H.; Nan, C. W. Enhanced thermoelectric properties of Bi$_2$O$_2$Se ceramics by Bi deficiencies. *J. Am. Ceram. Soc.* **2015**, *98*, 2465.

(11) Wu, J.; Tan, C. W.; Tan, Z. J.; Liu, Y. J.; Yin, J. B.; Dang, W. H.; Wang, M. Z.; Peng, H. L. Controlled synthesis of high-mobility atomically thin bismuth oxyselenide crystals. *Nano Lett.* **2017**, *17*, 3021.

(12) Meng, M.; Huang, S. Y.; Tan, C. W.; Wu, J. X.; Jing, Y. M.; Peng, H. L.; Xu, H. Q. Strong spin-orbit interaction and magneto-transport in semiconductor Bi$_2$O$_2$Se nanoplates. *Nanoscale* **2018**, *10*, 2704.

(13) Wu, J.; Liu, Y. J.; Tan, Z. J.; Tan, C. W.; Yin, J. B.; Li, T. R.; Tu, T.; Peng, H. L. Chemical patterning of high-mobility semiconducting 2D Bi$_2$O$_2$Se crystals for integrated optoelectronic devices. *Adv. Mater.* **2017**, *29*, No. 1704060.

(14) Li, J.; Wang, Z. X.; Wen, Y.; Chu, J. W.; Yin, L.; Cheng, R. Q.; Lei, L.; He, P.; Jiang, C.; Feng, L. P.; et al. High-performance near-infrared photodetector based on ultrathin Bi$_2$O$_2$Se nanosheets. *Adv. Funct. Mater.* **2018**, *28*, No. 1706437.

(15) Yu, J. B.; Sun, Q. Bi$_2$O$_2$Se nanosheet: An excellent high-temperature n-type thermoelectric material. *Appl. Phys. Lett.* **2018**, *112*, No. 053901.

(16) Wang, B.; Niu, X. H.; Ouyang, Y. X.; Zhou, Q. H.; Wang, J. L. Ultrathin semiconducting Bi$_2$Te$_2$S and Bi$_2$Te$_2$Se with high electron mobilities. *J. Phys. Chem. Lett.* **2018**, *9*, 487.

(17) Wu, M.; Zeng, X. C. Bismuth oxychalcogenides: a new class of ferroelectric/ferroelastic materials with ultra high mobility. *Nano Lett.* **2017**, *17*, 6309.

(18) Luu, S. D. N.; Vaqueiro, P. Synthesis, characterisation and thermoelectric properties of the oxytelluride Bi$_2$O$_2$Te. *J. Solid State Chem.* **2015**, *226*, 219.

(19) Zhang, X.; Liu, Y. F.; Zhang, G. H.; Wang, Y. Q.; Zhang, H.; Huang, F. Q. Thermal decomposition of bismuth oxysulfide from photoelectric Bi$_2$O$_2$S to superconducting Bi$_4$O$_4$S$_3$. *ACS Appl. Mater. Interfaces* **2015**, *7*, 4442.

(20) Ferrari, A. C. Raman spectroscopy of graphene and graphite: Disorder, electron-phonon coupling, doping and nonadiabatic effects. *Solid State Commun.* **2007**, *143*, 47.

(21) Pimenta, M. A.; del Corro, E.; Carvalho, B. R.; Fantini, C.; Malard, L. M. Comparative study of Raman spectroscopy in graphene and MoS$_2$-type transition metal dichalcogenides. *Acc. Chem. Res.* **2015**, *48*, 41.

(22) Zhang, S.; Zhang, N.; Zhao, Y.; Cheng, T.; Li, X. B.; Feng, R.; Xu, H.; Liu, Z. R.; Zhang, J.; Tong, L. M. Spotting the differences in two-dimensional materials - the Raman scattering perspective. *Chem. Soc. Rev.* **2018**, *47*, 3217.

(23) Jagło, G.; Medala, M.; Wdowik, U. D. Ab initio phonon dynamics in the layered ternary diselenide KNi$_2$Se$_2$. *Phys. Lett. A* **2015**, *379*, 183.

(24) Lazarević, N.; Radonjic, M.; Scepanovic, M.; Lei, H.; Tanaskovic, D.; Petrovic, C.; Popovic, Z. V. Lattice dynamics of KNi$_2$Se$_2$. *Phys. Rev. B* **2013**, *87*, No. 144305.

(25) Mittal, R.; Gupta, M. K.; Chaplot, S. L.; Zbiri, M.; Rols, S.; Schober, H.; Su, Y.; Brueckel, T.; Wolf, T. Spin-phonon coupling in K$_{0.8}$Fe$_{1.6}$Se$_2$ and KFe$_2$Se$_2$: Inelastic neutron scattering and ab initio phonon calculations. *Phys. Rev. B* **2013**, *87*, No. 184502.

(26) Guo, D. L.; Hu, C. G.; Xi, Y.; Zhang, K. Y. Strain effects to optimize thermoelectric properties of doped Bi$_2$O$_2$Se via Tran-Blaha Modified Becke-Johnson density functional theory. *J. Phys. Chem. C* **2013**, *117*, 21597.

(27) Mohiuddin, T. M. G.; Lombardo, A.; Nair, R. R.; Bonetti, A.; Savini, G.; Jalil, R.; Bonini, N.; Basko, D. M.; Galiotis, C.; Marzari, N.; et al. Uniaxial strain in graphene by Raman spectroscopy: G peak splitting, Gruneisen parameters, and sample orientation. *Phys. Rev. B* **2009**, *79*, No. 205433.

(28) Rice, C.; Young, R. J.; Zan, R.; Bangert, U.; Wolverson, D.; Georgiou, T.; Jalil, R.; Novoselov, K. S. Raman-scattering measurements and first-principles calculations of strain-induced phonon shifts in monolayer MoS$_2$. *Phys. Rev. B* **2013**, *87*, No. 081307.

(29) Zhang, S.; Mao, N. N.; Wu, J. X.; Tong, L. M.; Zhang, J.; Liu, Z. R. In-plane uniaxial strain in black phosphorus enables the identification of crystalline orientation. *Small* **2017**, *13*, No. 1700466.

(30) Li, Z. Z.; Liu, Z. F.; Liu, Z. R. Movement of Dirac points and band gaps in graphyne under rotating strain. *Nano Res.* **2017**, *10*, 2005.

(31) Wang, Y.; Cong, C.; Yang, W.; Shang, J.; Peimyoo, N.; Chen, Y.; Kang, J.; Wang, J.; Huang, W.; Yu, T. Strain-induced direct-indirect bandgap transition and phonon modulation in monolayer WS2. *Nano Res.* **2015**, *8*, 2562.

(32) Grimvall, G. *Thermophysical Properties of Materials*; North Holland, 1986.

(33) Wang, Y.; Cong, C. X.; Qiu, C. Y.; Yu, T. Raman spectroscopy study of lattice vibration and crystallographic orientation of monolayer MoS2 under uniaxial strain. *Small* **2013**, *9*, 2857.

(34) Giannozzi, P.; Baroni, S.; Bonini, N.; Calandra, M.; Car, R.; Cavazzoni, C.; Ceresoli, D.; Chiarotti, G. L.; Cococcioni, M.; Dabo, I.; et al. QUANTUM ESPRESSO: a modular and open-source software project for quantum simulations of materials. *J. Phys.: Condens. Matter* **2009**, *21*, No. 395502.

(35) Baroni, S.; de Gironcoli, S.; Dal Corso, A.; Giannozzi, P. Phonons and related crystal properties from density-functional perturbation theory. *Rev. Mod. Phys.* **2001**, *73*, 515.

(36) Tran, F.; Blaha, P. Accurate band gaps of semiconductors and insulators with a semilocal exchange-correlation potential. *Phys. Rev. Lett.* **2009**, *102*, No. 226401.

(37) Kresse, G.; Furthmuller, J. Efficiency of ab-initio total energy calculations for metals and semiconductors using a plane-wave basis set. *Comp. Mater. Sci.* **1996**, *6*, 15.

(38) Kresse, G.; Furthmuller, J. Efficient iterative schemes for ab initio total-energy calculations using a plane-wave basis set. *Phys. Rev. B* **1996**, *54*, 11169.

(39) Boller, H. Crystal-Structure of Bi_2O_2Se. *Monatsh. Chem.* **1973**, *104*, 916.

(40) Koyama, E.; Nakai, I.; Nagashima, K. Crystal-chemistry of oxide chalcogenides. II. synthesis and crystal structure of the first bismuth oxide-sulfide,Bi_2O_2S. *Acta Crystallogr., Sect. B: Struct. Sci.* **1984**, *40*, 105.

(41) Setyawan, W.; Curtarolo, S. High-throughput electronic band structure calculations: Challenges and tools. *Comput. Mater. Sci.* **2010**, *49*, 299.

(42) Pacquette, A. L.; Hagiwara, H.; Ishihara, T.; Gewirth, A. A. Fabrication of an oxysulfide of bismuth Bi_2O_2S and its photocatalytic activity in a Bi_2O_2S/In_2O_3 composite. *J. Photochem. Photobiol., A* **2014**, *277*, 27.

(43) Pereira, A. L. J.; Santamaría-Pérez, D.; Ruiz-Fuertes, J.; et al. Experimental and theoretical Study of Bi_2O_2Se under compression. *J. Phys. Chem. C* **2018**, *122*, 8853.

(44) Lazarević, N.; Lei, H. C.; Petrovic, C.; Popovic, Z. V. Phonon and magnon excitations in block-antiferromagnetic $K_{0.88}Fe_{1.63}S_2$. *Phys. Rev. B* **2011**, *84*, No. 214305.

(45) Lazarević, N.; Abeykoon, M.; Stephens, P. W.; Lei, H.; Bozin, E. S.; Petrovic, C.; Popovic, Z. V. Vacancy-induced nanoscale phase separation in $K_xFe_{2-y}Se_2$ single crystals evidenced by Raman scattering and powder x-ray diffraction. *Phys. Rev. B* **2012**, *86*, No. 054503.

(46) Jagło, G.; Wdowik, U. D. Lattice dynamics of a quasi-2D layered $TlCo_2Se_2$ with a helical magnetic structure. *RSC Adv.* **2016**, *6*, 79121.

(47) Zhang, J.; Peng, Z.; Soni, A.; Zhao, Y.; Xiong, Y.; Peng, B.; Wang, J.; Dresselhaus, M. S.; Xiong, Q. Raman Spectroscopy of Few-Quintuple Layer Topological Insulator Bi_2Se_3 Nanoplatelets. *Nano Lett.* **2011**, *11*, 2407.

(48) Zhao, Y. Y.; Luo, X.; Zhang, J.; Wu, J. X.; Bai, X. X.; Wang, M. X.; Jia, J. F.; Peng, H. L.; Liu, Z. F.; Quek, S. Y.; et al. Interlayer vibrational modes in few-quintuple-layer Bi_2Te_3 and Bi_2Se_3 two-dimensional crystals: Raman spectroscopy and first-principles studies. *Phys. Rev. B* **2014**, *90*, No. 245428.

(49) Ataca, C.; Topsakal, M.; Akturk, E.; Ciraci, S. A Comparative Study of Lattice Dynamics of Three- and Two-Dimensional MoS_2. *J. Phys. Chem. C* **2011**, *115*, 16354.

(50) Zhang, S. Q.; Wang, J. Y.; Li, Z. Z.; Zhao, R. Q.; Tong, L. M.; Liu, Z. F.; Zhang, J.; Liu, Z. R. Raman spectra and corresponding strain effects in graphyne and graphdiyne. *J. Phys. Chem. C* **2016**, *120*, 10605.

(51) Li, Z.; Wang, J. Y.; Liu, Z. R. Intrinsic carrier mobility of Dirac cones: The limitations of deformation potential theory. *J. Chem. Phys.* **2014**, *141*, No. 144107.

(52) Lang, H. F.; Zhang, S. Q.; Liu, Z. R. Mobility anisotropy of two-dimensional semiconductors. *Phys. Rev. B* **2016**, *94*, No. 235306.

(53) Wei, X. D.; Fragneaud, B.; Marianetti, C. A.; Kysar, J. W. Nonlinear elastic behavior of graphene: Ab initio calculations to continuum description. *Phys. Rev. B* **2009**, *80*, No. 205407.

(54) Cheng, T.; Lang, H. F.; Li, Z. Z.; Liu, Z. F.; Liu, Z. R. Anisotropic carrier mobility in two-dimensional materials with tilted Dirac cones: theory and application. *Phys. Chem. Chem. Phys.* **2017**, *19*, 23942.

(55) Qiao, J.; Kong, X. H.; Hu, Z. X.; Yang, F.; Ji, W. High-mobility transport anisotropy and linear dichroism in few-layer black phosphorus. *Nat. Commun.* **2014**, *5*, No. 4475.

(56) Thomsen, C.; Reich, S.; Ordejon, P. Ab initio determination of the phonon deformation potentials of graphene. *Phys. Rev. B* **2002**, *65*, No. 073403.